

A martian case study of segmenting images automatically for granulometry and sedimentology, Part 1: Algorithm



Suniti Karunatillake^{a,*}, Scott M. McLennan^b, Kenneth E. Herkenhoff^c, Jonathan M. Husch^d, Craig Hardgrove^e, J.R. Skok^a

^a Louisiana State University, E235 Howe–Russell, Baton Rouge, LA 70803, United States

^b Department of Geosciences, State University of New York at Stony Brook, Stony Brook, NY 11794, United States

^c U.S. Geological Survey, Astrogeology Science Center, Flagstaff, AZ 86001, United States

^d Department of Geological, Environmental, and Marine Sciences (GEMS), Rider University, 2083 Lawrenceville Road, Lawrenceville, NJ 08648, United States

^e Arizona State University, School of Earth and Space Exploration, Tempe, AZ 85287-1404, United States

ARTICLE INFO

Article history:

Available online 14 October 2013

Keyword:

Mars, surface

ABSTRACT

In planetary exploration, delineating individual grains in images via segmentation is a key path to sedimentological comparisons with the extensive terrestrial literature. Samples that contain a substantial fine grain component, common at Meridiani and Gusev at Mars, would involve prohibitive effort if attempted manually. Unavailability of physical samples also precludes standard terrestrial methods such as sieving. Furthermore, planetary scientists have been thwarted by the dearth of segmentation algorithms customized for planetary applications, including Mars, and often rely on sub-optimal solutions adapted from medical software. We address this with an original algorithm optimized to segment whole images from the Microscopic Imager of the Mars Exploration Rovers. While our code operates with minimal human guidance, its default parameters can be modified easily for different geologic settings and imagers on Earth and other planets, such as the Curiosity Rover's Mars Hand Lens Instrument. We assess the algorithm's robustness in a companion work.

© 2013 Elsevier Inc. All rights reserved.

1. Introduction

As an important recent achievement in sedimentology, orbital and surface observations have identified an extensive and highly varied sedimentary record on Mars (Grotzinger et al., 2011). Until samples are returned, however, the study of the physical sedimentology on Mars, including grain size analyses, must rely on high-resolution images. One example of such imaging involves the Mars Exploration Rover's (MER) Microscopic Imagers (MI) (Herkenhoff et al., 2003), carried onboard the Spirit and Opportunity rovers, that returned thousands of digital grayscale pictures with a resolution of 31 $\mu\text{m}/\text{pixel}$. The enormous time and resource commitment required for manual estimation of granulometry for such a large data set necessitates automated photoanalyses.

Here we present a new algorithm that delineates individual grains in sediment images by segmenting an image into binary values of objects and background; to our knowledge the first automated segmentation with minimal human guidance in planetary science (cf., Detert and Weitbrecht, 2012). We develop robust segmentation as the first step to comparisons of planetary data with established and extensive cumulative representations of terrestrial

sediment volume, mass, and shape (Boggs, 2009; Folk, 1968, 1980; Lewis and McConchie, 1994). We evaluate our algorithm and resulting code in our companion work (Karunatillake et al., 2013). A martian case study of segmenting images automatically for granulometry and sedimentology, Part 2: assessment, in press at Icarus).

Planetary images of sediment, martian MIs specifically, continue to need robust segmentation, mainly due to a lack of integration between mature algorithms used on Earth (e.g., Detert and Weitbrecht, 2012) and emerging planetary sedimentology. We bridge this gap by optimizing the methods used in several terrestrial fields for planetary science: bed surface sedimentology (Detert and Weitbrecht, 2012; Dugdale et al., 2010), hydrology (Strom et al., 2010), sediment core analyses (Lewis et al., 2010), and rock pile analyses in the mining industry (Franklin and Katsabanis, 1996). Instead of adopting commercial software used in such fields, such as Wipfrag, Simagis, and Fragscan (Maerz et al., 1996; Schleifer and Tessier, 2002), we developed a new algorithm to better suit planetary images for the reasons that follow.

First, segmentation typically – though not always, for example live tracking of sediment transport (Rubin et al., 2010) – plays a secondary role in studies of terrestrial sediment due to the ease of field access using sieves or methods such as grid-by-number (Graham et al., 2005b). Sieves in particular remain the gold

* Corresponding author. Fax: +1 (225) 578 2302.

E-mail address: wk43@cornell.edu (S. Karunatillake).

standard on Earth, even in the mining industry where image segmentation is necessary to assess size distributions of blasted rock piles (Maerz et al., 1996). In contrast, image analysis remains the only tool available to planetary sedimentologists.

Second, our own work (Karunatillake et al., 2010) demonstrated many deficiencies to manual segmentation. For example, subsections of images, even when selected as representative of the whole, frequently differed in the distribution of grain sizes. Manual delineation of individual grains became impractically slow with the preponderance of grains finer than few tens of pixels across. This became an acute issue for fine grains proximal to others larger by more than an order of magnitude. Furthermore, internal consistency of manual segmentation seemed suspect, challenged by both positioning and grain perimeter precision.

Third, we did not find compelling automated alternatives in the planetary science literature. Most of our peers rely on ImageJ, developed specifically for medical image analyses (e.g., Lewis et al., 2010), to semi-automate segmentation of images from MER and Phoenix missions (Cabrol et al., 2008; Calvin et al., 2008; Goetz et al., 2010; Yingst et al., 2008). More important, the slowest task of delineating grain edges was done manually, while software assumed the secondary role of computing grain dimensions and size–frequency analyses (Goetz et al., 2010; Yingst et al., 2008). Even when conducted on a robust grid-by-number basis that allows direct comparison with terrestrial granulometry (McGlynn et al., 2011, 2012), this approach remains slow due to segmenting manually.

Fourth, automated alternatives used on Earth are often statistical (Barnard et al., 2007; Buscombe et al., 2010; Rubin, 2004), returning summary parameters via Fourier decomposition for example, unlike geometric methods that would identify individual grains with detailed areal analyses of grain size distributions. Geometric methods targeted at river bed sediments in the context of hydrological modeling (e.g., Detert and Weitbrecht, 2012) often operate on grain populations with less size contrast between coarse and fine grain components than typical of martian images.

Finally, we sought to identify the limits of segmentation; both the finest grains that can be identified while retaining accuracy on the order of ~10%, and the largest grains whose distribution can be sampled sufficiently given the Field of View (FOV) of the imager. In addition, we identify issues that plague segmentation and their implications to our algorithm.

2. Method

Given the objective of developing an algorithm to automatically segment images from Mars, specifically from the MER MIs, we describe the algorithm with sufficient detail to code in any software platform, including a summary flowchart. Our companion work (Karunatillake et al., 2013, submitted for publication) describes its assessment.

The spatial resolution of photoanalysis – automated or manual – depends solely on the imaging device; for example, 2 pixels would correspond nominally to 62 μm for MI images. Throughout the text, we list such examples with linear size and Wentworth classification in parenthesis for MI images, such as 2 pixels (MI: 62 μm , coarse silt), to provide context. However, the effective resolution may often differ, depending on the desired accuracy of size for smaller grains and of distribution for larger grains. We express such constraints in image pixels to facilitate resolution estimates for any imager, as the product of pixel size and the linear dimension of the image in pixels. In Section 3.1 we also present examples in Φ , SI units, and corresponding Wentworth classes for current planetary instruments.

The algorithm (Fig. 1) has several key manual guide points that exploit the extraordinary pattern recognition abilities of the human brain (e.g., Bharath and Petrou, 2008). The first is the

qualitative visual aspect of grains positioned atop, closer to the imager, or generally distinct and fewer in number than most grains in the image. We abbreviate the subset of such grains as the image “foreground.” Fig. 1 contrasts an MI image where the foreground is distinct from the background, with one where it is not. In MI images, those with distinct foregrounds typically have larger grains atop finer grains, yielding clear qualitative differences in illumination, shadows, and texture. Images of well-sorted grains, El Dorado sand for example (Sullivan et al., 2008), typically have indistinguishable foregrounds. The choice, reversible should the outcome dissatisfy the human operator, is binary: the foreground is either distinct or it is not.

2.1. Image prepared

The algorithm bifurcates according to the choice of foreground type (Fig. 1 Steps 2 and 3, denoted subsequently as 1S2 and 1S3 for brevity). For the case of a distinct foreground, the next step is gamma correction, available in all image processing software (e.g., pp. 260, 630 by Poynton, 2002), to brighten darker regions. The resulting image is processed in two different ways: One blurs unusual features – such as sharp geometric shapes – with erosion (e.g., Gonzalez and Woods, 2007) using a disk matrix of 3-pixel radius (Fig. 1S2.1.1). The size of the disk matrix was determined empirically using several MI images, and remains adjustable to suit different data sources, such as the Phoenix mission’s Robotic Arm Camera (RAC) (Keller et al., 2008) or the microscope of MECA (Microscopy, Electrochemistry, and Conductivity Analyzer) (Hecht et al., 2008).

The other path computes the information entropy (e.g., Havil and Dyson, 2003) for each pixel using the 8 nearest neighboring pixels (Fig. 1S2.1.2). This exploits the textured nature of the background relative to the foreground, with accordingly higher entropy values. The result is scaled to the grayscale [0, 1] range, clipped to between [0, 0.5], then dilated (e.g., Dougherty and Lotufo, 2003) to minimize holes and irregularities in the isolated foreground objects. The two images that result, one from erosion and the other from entropy filtering, are added linearly after the entropy filtered image is multiplied by 0.2. The 0.2 weight was determined manually using several MI images, and can be adjusted for data from other instruments. The resulting image is scaled yet again to between 0 and 1, yielding Fig. 1c. Polychromatic images are processed in grayscale since the color information does not usually yield better segmentation despite increasing the complexity of analysis (e.g., para. 11 by Graham et al., 2005c). The entropy filter steps makes our algorithm distinct from others such as the segmentation method by Detert and Weitbrecht (2012).

2.2. Foreground segmented

The next step (Fig. 1S2.3) is key to segmenting foreground objects successfully. We employ Mathematica’s inbuilt module that uses Otsu’s algorithm (1979) maximizing cluster variance to compute a global threshold, t , in pixel intensity (i.e., grayscale). Segmentation is then achieved morphologically, modulated with two scale factors that the operator submits (Fig. 1S2.4), c and f , where $f \geq c$. The algorithm uses $f \times t$ as the threshold grayscale value above which a pixel is assigned to the foreground with a value of 1. The lower threshold $c \times t$ allows pixels connected to foreground objects to be included in the foreground despite failing to satisfy the global ft threshold. This ensures local contiguity of grains, minimizing fragmentation (Eden and Franklin, 1996), for example, while minimizing the variance of pixel intensity within each area defined as a single grain. An operator can modify f and c iteratively until the segmented image appears satisfactory; the process is aided by a visually striking change of the output at the transition from sub-optimal values to the optimal value.

software environments as a standard module. A key difference from morphological components algorithms such as by Otsu (1979) (Fig. 1S2.3) is that Watershed assesses the image much like a terrestrial elevation map of aqueous watersheds by first identifying minima, then expanding across neighboring pixels of least value up to an optimal level. This maximizes the area of grains while restricting the background to grain boundaries; as a consequent drawback, the majority of pixels are segmented, with a high likelihood of fragmentation and improper classification of pore space as parts of grains.

Unlike the use of Watershed segmentation as a final step by other workers (e.g., Detert and Weitbrecht, 2012), we avoid Watershed's tendency to hyper-segment by employing Watershed's binary image output (Fig. 1S3.6) solely to highlight potential grain boundaries. We achieve this by multiplying the Watershed Image (Fig. 1S3.6) with its initial opened counterpart (Fig. 1S3.4); pixels assigned zero by Watershed become zero in the final image, while others retain their values. At this point, the image can be segmented morphologically without additional morphological transformations such as Bottom-Hat, or edge detections such as Sobel (c.f., Detert and Weitbrecht, 2012); without Watershed, an algorithm such as Otsu's would have fused too many distinct grains. To minimize fused grains further, unlike Fig. 1S2.5, the secondary threshold for connected neighbors is absent. However, the primary multiple of the segmentation threshold t remains adjustable by the operator as $f/2$. The binary image that results from the segmentation reveals background grains optimally.

As shown in Fig. 1S4, whenever the foreground appears distinct to the operator, the final segmented image is the addition of that from Fig. 1S2.9 with that from Fig. 1S3.10, yielding the final segmented image (Fig. 1e). In all others instances, only the second branch of the algorithm is executed as just described. As described in the preceding paragraphs, Fig. 1a–e shows the appearance of an example MI image at several key steps.

Standard software options allow grain dimensions to be measured individually in a binarized image, which can then feed an automated granulometry code. We may achieve this with the module "ComponentMeasurements" in the Mathematica-8 environment, which automatically computes the weighted area of each grain. It also computes the major and minor semi-axes of the best fit ellipse, determined in a manner that yields the most accurate measure in empirical observations: second moment of area (Graham et al., 2005a).

3. Results and discussion

While we do not endorse Mathematica over alternatives, Mathematica-8 offered us the advantage of an inbuilt inventory of all the key modules of the algorithm, requiring mostly concatenation to create the software. Additional strengths include the ability to seamlessly assign numeric and non-numeric values to variables; to achieve precision independent of the hardware environment; to annotate results with rich text; and to evaluate interactively with the GUI module, "Manipulate". These benefits are enhanced further at the granulometry phase, given the availability of exhaustive measures of grain form and shape with a component descriptor module "ComponentMeasurements." We include the function modules as a supplementary Mathematica file with this manuscript for future applications by other scientists.

Visually, the algorithm segmented the whole image impressively, examples of which are shown in Fig. 2 for cases of both distinct and indistinct foreground. We describe the evaluation of the algorithm in our companion work (Karunatilake et al., 2013, submitted for publication). In this work, we describe the broader grain size thresholds of photoanalysis that apply to our algorithm.

Photoanalysis in general and segmentation in particular is subject to two important thresholds: at the smallest grain sizes, with the challenge to measure the diameter correctly; and at the largest grain sizes, with the challenge to sample the distribution correctly. Empirical assessments with terrestrial sediments (Graham et al., 2005c, 2010) as well as with synthetic spheres (Kennedy and Mazzullo, 1991) have characterized these values as a function of the number of pixels in an image and of the size of a grain in pixels. Knowing the spatial resolution of the image in length/pixel, such thresholds convert directly to length via (pixels) \times (size of a pixel). As before, for general applicability with all imaging devices, we state thresholds as reported in pixels by other sedimentologists, followed by the MI equivalent within parenthesis as a concrete example in the geologic context of soil at Gusev and Meridiani.

3.1. Smallest grain size

Using coarse-grained sediments easily resolvable to a human, Graham et al. (2005a) – in their Fig. 9 – have shown that the algorithmic measure of grain diameter can be inaccurate by more than 5% at the smallest 5th percentile of the distribution when the minor full axis is less than about 23 pixels in size (MI: 713 μm , coarse sand, where a 5% error would still preserve the Wentworth classification). However, the middle range of the distribution appears generally unaffected. Nevertheless, the 23 pixel size (MI: 713 μm , coarse sand) also appears optimal for manual segmentation due to factors Graham et al. (2005a) enumerate as: (1) increase in proportional significance of each pixel at smaller diameters (2) location uncertainty of boundary pixels (3) boundary uncertainty of adjacent pixels (cf., para. 16 by Graham et al., 2010). We note that this size threshold contrasts starkly with the optimistic value of approximately 5 pixels (MI: 155 μm , fine sand) that has been used in recent planetary literature (e.g., Karunatilake et al., 2010). Such fine thresholds may be robust only for summary statistical parameters (Rubin, 2004; Rubin et al., 2007, 2010).

Using spheres of known size, Kennedy and Mazzullo (1991) also demonstrated that the estimated diameter of a sphere can be in error by $\sim 10\%$ when the perimeter is less than 8 pixels (equivalent to 2.5 pixel diameter; MI: 78 μm , very fine sand. The correct classification is retained up to a 17% error, at which point an incorrect Wentworth classification of silt would result), which decreases to $\sim 1\%$ when the perimeter exceeds 22 pixels (equivalent to 7.0 pixel diameter; MI: 217 μm , fine sand). For an imager with variable focal length, such as RAC (Keller et al., 2008) or MAHLI (Edgett et al., 2009, 2012), it is possible to consider the size threshold either as the smallest size that can be measured accurately or as the largest area that may be imaged with acceptable error in the smallest desired grain size. Different thresholds apply for grain form properties such as convexity and roundness (Roussillon et al., 2009). These thresholds (Table 1) may also be converted (para. 9 by Graham et al., 2005c) to yield smallest grain diameter in μm as a function of imaged area (A in mm^2), number of pixels in image (P), and smallest diameter in pixels (n): $(10^3 n \sqrt{\frac{A}{P}})$.

Some of the thresholds in Table 1 applied for MAHLI ($\sim 13.9 \mu\text{m}/\text{pixel}$, scale of fine silt at maximum magnification for 1600×1200 pixel image), MI ($\sim 30 \mu\text{m}/\text{pixel}$, scale of medium silt, fixed focus for 1024×1024 pixel image), MECA ($\sim 4 \mu\text{m}/\text{pixel}$, scale of very fine silt, fixed focus for 256×512 pixel image (para. 15 by Hecht et al., 2008)), and RAC ($\sim 23 \mu\text{m}/\text{pixel}$, scale of medium silt at maximum magnification for 256×512 pixel image (para. 17 by Keller et al., 2008)) images are shown in Fig. 3. Comparatively, MAHLI's potential limit of $\sim 325 \mu\text{m}$ (medium sand) indicates a major improvement over MI's $\sim 700 \mu\text{m}$ (coarse sand) as evident in Fig. 3(Top).

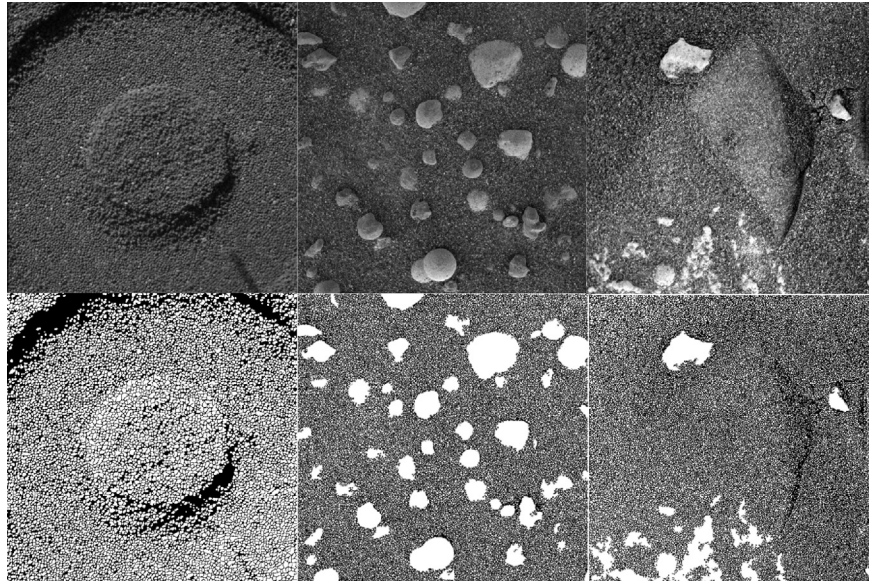


Fig. 2. Examples of MI images segmented with the Mathematica-8 application of our algorithm. Original images are shown above the corresponding binary images. From left to right: sol 709 at Gusev, sol 17 at Meridiani, and sol 38 at Meridiani.

Table 1
Smallest segmented grain for which a particular aspect is accurate at a specified level, with diametric size specified in pixels. These thresholds generate the curves shown in Fig. 3 for variable-focus imagers.

Aspect	Error limiting description	Smallest diameter in pixels {MI equivalent size}	Reference
Grain diameter	<5% relative to physical measurement of the smallest 5th percentile of grains	23 {713 μm , coarse sand}	Graham et al. (2005a, Fig. 9)
Grain diameter	<4% for ellipse-fit method relative to direct iterative method	12 {372 μm , medium sand}	Graham et al. (2005a, Fig. 13)
Grain perimeter length	<10% relative to known value of sphere	2.5 equivalent {78 μm , very fine sand} (perimeter ≥ 8 pixels)	Kennedy and Mazzullo (1991, Table 6.1)
Roundness	<5% relative to physical measurement	16 equivalent {496 μm , medium sand} (perimeter ≥ 50)	Roussillon et al. (2009, Fig. 7)
Convexity	<5% relative to physical measurement	32 equivalent {992 μm , coarse sand} (perimeter ≥ 100)	Roussillon et al. (2009, Fig. 7)
Physical resolvability	Point spread function for CCD	~ 0.8 – 1.5 {25–47 μm , medium to coarse silt}; varies with instrument	McEwen et al. (2007, para. 17 and Fig. 9)
Planetary community use	Experiential and qualitative limit to manual segmentation	5 {155 μm , fine sand}	Karunatilake et al. (2010, para. 12 and 13)

3.2. Sampling the size distribution

The upper bound in size threshold reflects the difficulty of sampling a distribution unless a minimum number of grains are present in the field of view. Consequently, it may be computed as a bound on the largest grain size that may be sampled correctly. Alternatively, where variable focus or image mosaics are available, it can be the minimum FOV area required to sample a particular upper bound on grain size. As Graham et al. (2010, Figs. 2 and 3, and Table 1) determined empirically, the diameter corresponding to the largest 10th percentile of the distribution can be estimated within 10% accuracy if the FOV area is at least $\times 100$ that of the largest grain. This also corresponds to an error not more than 5% at the median size. An error not exceeding 10% at the median is possible with the FOV $\times 50$ that of the largest grain size. For greater accuracy on the order of 5% in the largest 10th percentile, the FOV area would need to be $\times 200$ that of the largest grain. As with the finest grain size, these thresholds can be presented graphically (Fig. 4) to determine the necessary FOV or mosaic size for a given set of image properties. Likewise, the thresholds apply readily for an image of known properties – size of each pixel and the number

of pixels along each dimension of the image. Alternatively, for a device with variable focal length and object distance, such as MAHLI (Edgett et al., 2012), the FOV area may be computed directly using the lens formula (p. 732 by Knight, 2007) as $d_1 d_2 (\frac{s}{f} - 1)^2$ where d_1 and d_2 are the linear dimensions of the CCD, s is the object distance, and f the focal length. In either case, the calculation remains independent of the compression ratio of the image and bits per pixel, since they contribute to the precision with which the image may be segmented rather than the accuracy.

4. Conclusions and future work

Our algorithm segments images of unconsolidated sediment automatically while allowing manual control, first by assessing whether the image has a distinct foreground and subsequently by fine-tuning the parameters of segmentation. As discussed in our companion work (Karunatilake et al., 2013, submitted for publication), it enables a degree of internal consistency and rapidity likely unachievable manually by a sedimentologist. The software implementation of our algorithm can be accompanied by automated granulometry, further reducing the task complexity for

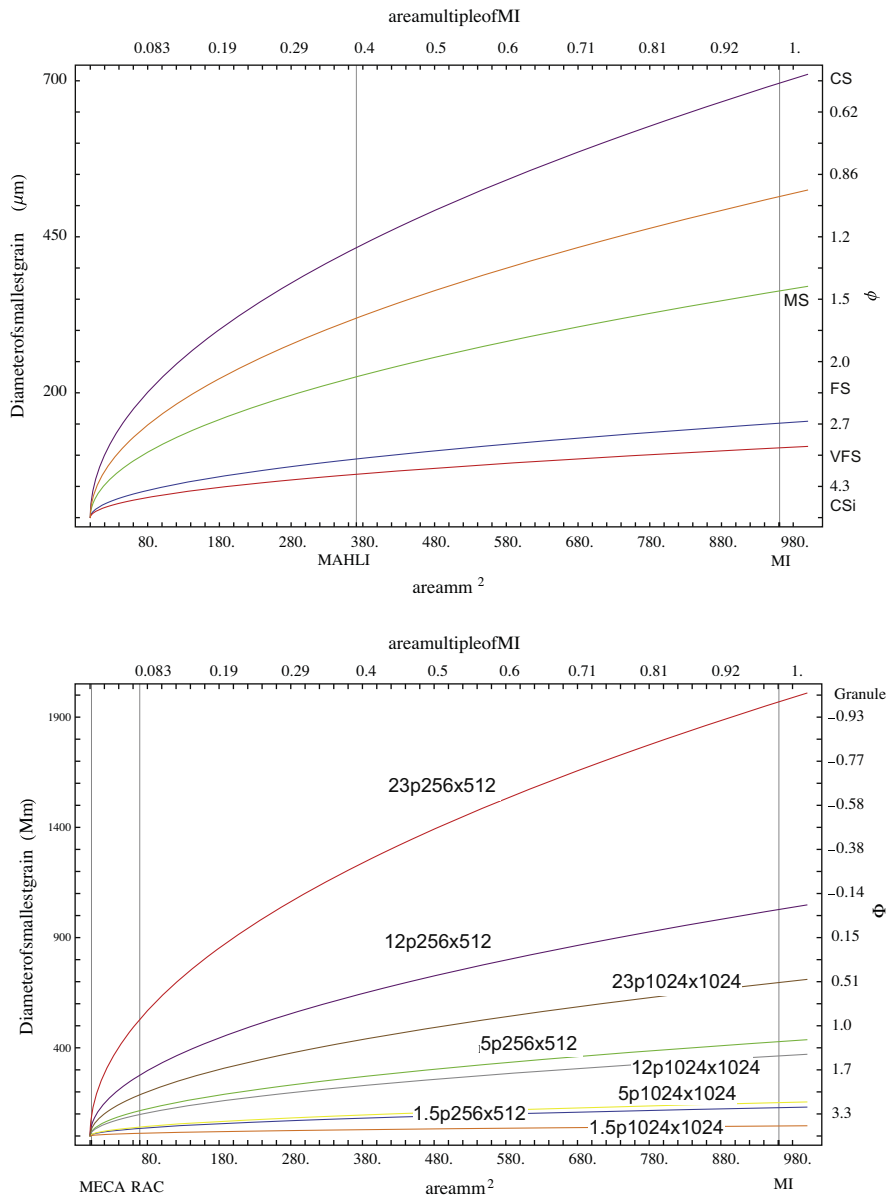


Fig. 3. Diameter of smallest measurable grain as a function of the FOV area (mm^2) for different image sizes (total number of pixels) and grain properties. Curves assume variable focus, with MAHLI limit identified by the intersection with vertical gridline labeled “MAHLI,” (upper plot) and the fixed MI limit by the label “MI.” FOV relative to the area of an MI image is shown in the upper abscissa, while the lower indicates area in mm^2 . Left ordinate is diameter in μm , while the right ordinate lists Φ units (CS: coarse sand; MS: medium sand; FS: fine sand; VFS: very fine sand; CSi: coarse silt). 1024×1024 pixel FOVs (e.g., MI type) are blue (5 pixel threshold), green (12), and purple (23). 1600×1200 pixel FOVs (e.g., MAHLI-type) are red (5 pixels) and orange (23). Accuracy level and context corresponding to each threshold is listed in Table 1. Lower plot shows additional thresholds from Table 1, where the label 5p256 \times 512 for example refers to the 5 pixel threshold with image size 256 \times 512 pixels and variable focus. As discussed in Section 3.1, 256 \times 512 pixel image sizes correspond to RAC and MECA instruments. (For interpretation of the references to color in this figure legend, the reader is referred to the web version of this article.)

planetary sedimentology. A notable strength of the automated granulometric implementation is the computation of areal distributions as an approximation to bulk distributions in terrestrial analog literature. We intend to expand the granulometric component of the software further to include grain form characterization such as convexity, roundness, and elongation (Roussillon et al., 2009) in upcoming work.

Our algorithm compares favorably with the independent sophisticated segmentation algorithm implemented in the MATLAB platform by Detert and Weitbrecht (2012) for fluvial bed grain analyses. Their work exemplifies the utility of a Graphical User Interface (GUI) with robustness for terrestrial gravel photos, and upward scalability similar to ours. Both techniques reinforce the

use of Otsu's, Watershed, erosion, and dilation algorithms. Detert and Weitbrecht (2012) software advances our code in several ways. First, their GUI offers intuitive operation without a need to type commands. Second, the GUI interface applies segmentation selectively to different parts of the image. Third, their judicious use of Canny and Sobel edge detection with Bottom Hat transforms may strengthen operation.

Our algorithm advances the approach by Detert and Weitbrecht (2012) in several ways: (1) we employ gamma correction to minimize shadowing data loss; (2) we distinguish large grains from fine grains on a textural basis with an entropy filter. This allows operating on fine grains separately, which are much harder to segment than large grains; (3) the dual-method of our code may successfully

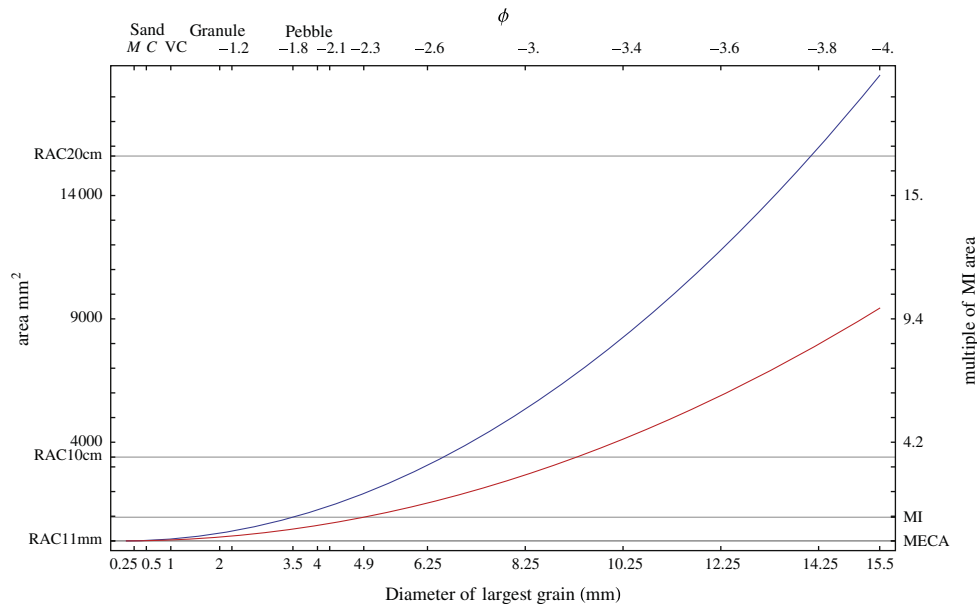


Fig. 4. Relationship between diameter of largest grain in image and imaged area (mm^2) to achieve desired accuracy. Curve in blue is for 10% accuracy in the diameter corresponding to the largest 10th percentile. This also corresponds to an error not more than 5% at the median size. Red curve reflects an error not exceeding 10% at the median. Intersections of the curves and horizontal lines reveal size thresholds for the RAC at maximum magnification (11 mm distance to object, 10 cm distance to object, and 20 cm distance to object). Intersection with lines labeled MECA and MI show thresholds for the corresponding fixed-focus instruments. The upper abscissa lists grain size in Φ units and classes (M, C, and VC indicate medium, coarse, and very coarse sand, respectively), and the right ordinate the FOV in mm^2 . Calculation discussed in Section 3.2. (For interpretation of the references to color in this figure legend, the reader is referred to the web version of this article.)

segment at higher orders of size difference across grains in a sample. Lastly, we present our algorithm in a manner encouraging independent coding and assessment. Summarily, while the two techniques rely fundamentally on reflectance properties, they cater to different sedimentological communities. However, using the two methods concurrently may allow insight comparable to that gained from manual segmentation by two independent teams.

As we discuss in our companion manuscript (Karunatillake et al., 2013, submitted for publication), we will address the major caveat of our work, the physical inaccessibility of martian sediment, by using terrestrial analogs in an upcoming project. Entailing sieving for uniformity of samples, this would effectively calibrate our algorithm independent of human vision. We will also consider diverse examples analyzing terrestrial sediment as references to compare with sieved results, assess previous planetary granulometry with MER MIs (Karunatillake et al., 2010; McGlynn et al., 2011), and determine grain size distributions in the context of Thermal Infrared characterization (Ferguson et al., 2006; Hardgrove et al., 2009). Possible application to petrological thin sections could also be considered, as could applications in other terrestrial settings where sediment would be digitally imaged (e.g., Roussillon et al., 2009). Using robotically generated images to assess undisturbed shallow sediment of deep sea and lake beds would be an additional use that would complement current physical sampling methods (e.g., Goff et al., 2004; Leduc et al., 2012; Litt et al., 2009; Valloni and Maynard, 1981).

The automated segmentation described in this manuscript may provide input for software currently used by planetary scientists, such as adaptations of ImageJ. While the segmentation algorithm can be implemented in any software environment such as IDL and R, our particular implementation in Mathematica-8 offers access to a rich suite of features, including the “ComponentMeasurements” module enabling seamless automation of granulometry. Stability and speed also result from the inbuilt availability of all necessary function modules. Finally, the software implementation is supported by Wolfram Inc., ensuring long-term viability of the code with an established technology partner.

Acknowledgments

Peter Overmann, Shadi Ashnai, Theodore Gray, and other members of the Wolfram Research Image Processing Team provided analytical and coding solutions to key hurdles, without which we would have been unsuccessful in developing our algorithm. We thank Dave Rubin and Aileen Yingst for vital feedback on an earlier version of the manuscript, which also helped to clarify our path for future research. We were supported by NASA Mars Data Analysis Program Grants NNX07AN96G, NNX10AQ23G, NNZ11AI94G, and NNX13AI98G. Louisiana State University’s Geology and Geophysics Department in the College of Science provided postdoctoral funding to support J.R. Skok. Undergraduate students Jade Bing, Jacqueline Bleakley, Thomas Vajtay, and Thomas Weindl at Rider University provided helpful suggestions, enhancing the readability of our work.

References

- Barnard, P.L., Rubin, D.M., Harney, J., Mustain, N., 2007. Field test comparison of an autocorrelation technique for determining grain size using a digital “beachball” camera versus traditional methods. *Sediment. Geol.* 201, 180–195.
- Bharath, A.A., Petrou, M., 2008. Next Generation Artificial Vision Systems: Reverse Engineering the Human Visual System. Artech House, Norwood, MA.
- Boggs, S., 2009. Petrology of Sedimentary Rocks. Cambridge University Press.
- Buscombe, D., Rubin, D.M., Warrick, J.A., 2010. A universal approximation of grain size from images of noncohesive sediment. *J. Geophys. Res.* 115, F02015.
- Cabrol, N.A. et al., 2008. Soil sedimentology at Gusev crater from Columbia Memorial Station to Winter Haven. *J. Geophys. Res.* 113, E06S05.
- Calvin, W.M. et al., 2008. Hematite spherules at Meridiani: Results from MI, Mini-TES, and Pancam. *J. Geophys. Res.* 113, E12S37.
- Detert, M., Weitbrecht, V., 2012. Automatic object detection to analyze the geometry of gravel grains – A free stand-alone tool. In: Murillo (Ed.), *River Flow 2012*. Taylor & Francis, London, pp. 595–600.
- Dougherty, E.R., Lofufo, R.A., 2003. *Hands-on Morphological Image Processing*. SPIE Publications.
- Dugdale, S.J., Carbonneau, P.E., Campbell, D., 2010. Aerial photosieving of exposed gravel bars for the rapid calibration of airborne grain size maps. *Earth Surf. Process. Landforms* 35, 627–639.
- Eden, D.J., Franklin, J.A., 1996. Disintegration, fusion, and edge net fidelity. In: Franklin, J., Katsabanis, T. (Eds.), *Fragblast-5 Workshop on Measurement of Blast Fragmentation*, Rotterdam, Montréal, Québec, Canada, pp. 127–132.

- Edgett, K.S. et al., 2009. The Mars Science Laboratory (MSL) Mars Hand Lens Imager (MAHLI) Flight instrument. *Lunar Planet. Sci.* p. 1197.
- Edgett, K.S. et al., 2012. Curiosity's Mars Hand Lens Imager (MAHLI) Investigation. *Space Sci. Rev.* 170, 259–317.
- Ferguson, R.L., Christensen, P.R., Bell, J.F., Golombek, M.P., Herkenhoff, K.E., Kieffer, H.H., 2006. Physical properties of the Mars Exploration Rover landing sites as inferred from Mini-TES-derived thermal inertia. *J. Geophys. Res.* 111, E02S21.
- Folk, R.L., 1968. *Petrology of Sedimentary Rocks: The University of Texas Geology* 370K, 383L, 383M. Hemphill, Austin, TX.
- Folk, R.L., 1980. *Petrology of Sedimentary Rocks*. Hemphill, Austin, TX.
- Franklin, J., Katsabanis, T., 1996. Measurement of blast fragmentation. In: *Proceedings of the Fragblast-5 Workshop on Measurement of Blast Fragmentation*, Rotterdam, Montréal, Québec, Canada, 23–24 August 1996.
- Goetz, W. et al., 2010. Microscopy analysis of soils at the Phoenix landing site, Mars: Classification of soil particles and description of their optical and magnetic properties. *J. Geophys. Res.* 115, E00E22.
- Goff, J.A. et al., 2004. Seabed characterization on the New Jersey middle and outer shelf: Correlatability and spatial variability of seafloor sediment properties. *Mar. Geol.* 209, 147–172.
- Gonzalez, R.C., Woods, R.E., 2007. *Digital Image Processing*, third ed. Prentice Hall.
- Graham, D.J., Reid, I., Rice, S.P., 2005a. Automated sizing of coarse-grained sediments: Image-processing procedures. *Math. Geol.* 37, 1–28.
- Graham, D.J., Rice, S.P., Reid, I., 2005b. Comment: Photographic techniques for characterizing streambed particle sizes. *Trans. Am. Fish. Soc.* 134, 1599–1603.
- Graham, D.J., Rice, S.P., Reid, I., 2005c. A transferable method for the automated grain sizing of river gravels. *Water Resour. Res.* 41, W07020, <http://dx.doi.org/10.1029/2004WR003868>.
- Graham, D.J., Rollet, A.-J., Piégay, H., Rice, S.P., 2010. Maximizing the accuracy of image-based surface sediment sampling techniques. *Water Resour. Res.* 46, W02508, <http://dx.doi.org/10.1029/2008WR006940>.
- Grotzinger, J. et al., 2011. Mars sedimentary geology: Key concepts and outstanding questions. *Astrobiology* 11, 77–87.
- Hardgrove, C., Moersch, J., Whisner, S., 2009. Thermal imaging of alluvial fans: A new technique for remote classification of sedimentary features. *Earth Planet. Sci. Lett.* 285, 124–130.
- Havil, J., Dyson, F., 2003. A measure of uncertainty. In: *Gamma: Exploring Euler's Constant*. Princeton Science Library, Princeton, NJ, pp. 139–145.
- Hecht, M.H. et al., 2008. Microscopy capabilities of the Microscopy, Electrochemistry, and Conductivity Analyzer. *J. Geophys. Res.* 113, E00A22.
- Herkenhoff, K.E. et al., 2003. Athena Microscopic Imager investigation. *J. Geophys. Res.* 108, <http://dx.doi.org/10.1029/2003JE002076>.
- Karunatillake, S., McLennan, S.M., Herkenhoff, K.E., 2010. Regional and grain size influences on the geochemistry of soil at Gusev crater, Mars. *J. Geophys. Res.* 115, E00F04.
- Keller, H.U. et al., 2008. Phoenix Robotic Arm Camera. *J. Geophys. Res.* 113, E00A17.
- Kennedy, S.K., Mazzullo, J., 1991. *Image analysis method of grain size measurement. Methods and Application of Particle Size Analysis*. Cambridge University Press.
- Knight, R.D., 2007. *Physics for Scientists and Engineers: A Strategic Approach with Modern Physics and Mastering Physics*, second ed. Addison-Wesley.
- Leduc, D. et al., 2012. Further evidence for the effect of particle-size diversity on deep-sea benthic biodiversity. *Deep Sea Res. I: Oceanogr. Res. Pap.* 63, 164–169.
- Lewis, D.W., McConchie, D.M., 1994. *Analytical Sedimentology*. Chapman Hall, New York, NY, United States.
- Lewis, T., Francus, P., Bradley, R.S., Kanamaru, K., 2010. An automated system for the statistical analysis of sediment texture and structure at the micro-scale. *Comput. Geosci.* 36, 1374–1383.
- Litt, T. et al., 2009. "PALEOVAN", International Continental Scientific Drilling Program (ICDP): Site survey results and perspectives. *Quatern. Sci. Rev.* 28, 1555–1567.
- Maerz, N.H., Palangio, T.C., Franklin, J.A., 1996. WipFrag image based granulometry system. In: Franklin, J., Katsabanis, T. (Eds.), *Measurement of Blast Fragmentation: Proceedings of the Fragblast-5 Workshop on Measurement of Blast Fragmentation*, Rotterdam, Montréal, Québec, Canada, 23–24 August 1996, pp. 91–99.
- McEwen, A.S. et al., 2007. Mars Reconnaissance Orbiter's High Resolution Imaging Science Experiment (HiRISE). *J. Geophys. Res.* 112, E05S02.
- McGlynn, I.O., Fedo, C.M., McSween, H.Y., 2011. Origin of basaltic soils at Gusev crater, Mars, by aeolian modification of impact-generated sediment. *J. Geophys. Res.* 116, E00F22.
- McGlynn, I.O., Fedo, C.M., McSween, H.Y., 2012. Soil mineralogy at the Mars Exploration Rover landing sites: An assessment of the competing roles of physical sorting and chemical weathering. *J. Geophys. Res.* 117, E01006.
- Meyer, F., 1994. Topographic distance and watershed lines. *Signal Process.* 38, 113–125.
- Otsu, N., 1979. A threshold selection method from gray-level histograms. *IEEE Trans. Syst. Man Cybernet.* 9, 62–66.
- Poynton, C., 2002. *Digital Video and HDTV: Algorithms and Interfaces*. Morgan Kaufmann.
- Roussillon, T., Piégay, H., Sivignon, I., Tougne, L., Lavigne, F., 2009. Automatic computation of pebble roundness using digital imagery and discrete geometry. *Comput. Geosci.* 35, 1992–2000.
- Rubin, D.M., 2004. A simple autocorrelation algorithm for determining grain size from digital images of sediment. *J. Sediment. Res.* 74, 160–165.
- Rubin, D.M., Chezar, H., Harney, J.N., Topping, D.J., Melis, T.S., Sherwood, C.R., 2007. Underwater microscope for measuring spatial and temporal changes in bed-sediment grain size. *Sediment. Geol.* 202, 402–408.
- Rubin, D.M. et al., 2010. New technology for in situ grain-size analysis from digital images of sediment, and resulting insights regarding sediment transport. In: *2nd JFIC*, Las Vegas, NV.
- Schleifer, J., Tessier, B., 2002. Fragmentation assessment using the FragScan system: Quality of a blast. *Fragblast* 6, 321–331.
- Strom, K.B., Asce, M., Kuhns, R.D., Lucas, H.J., 2010. Comparison of automated image-based grain sizing to standard pebble-count methods. *J. Hydraul. Eng.* 136, 461–473.
- Sullivan, R. et al., 2008. Wind-driven particle mobility on Mars: Insights from Mars Exploration Rover observations at "El Dorado" and surroundings at Gusev crater. *J. Geophys. Res.* 113, E06S07.
- Valloni, R., Maynard, J.B., 1981. Detrital modes of recent deep-sea sands and their relation to tectonic setting: A first approximation. *Sedimentology* 28, 75–83.
- Yingst, R.A., Crumpler, L., Farrand, W.H., Li, R., Cabrol, N.A., Neakrase, L.D., 2008. Morphology and texture of particles along the Spirit rover traverse from sol 450 to sol 745. *J. Geophys. Res.* 113, E12S41.